Macromolecules

pubs.acs.org/Macromolecules Article

Supernucleation Dominates Lignin/Poly(ethylene oxide) Crystallization Kinetics

María E. Taverna, Abdullah S. Altorbaq, Sanat K. Kumar,* Jorge L. Olmedo-Martínez, Carlos A. Busatto, Manuela Zubitur, Agurtzane Mugica, Verónica V. Nicolau, Diana A. Estenoz, and Alejandro J. Müller*

Cite This: *Macromolecules* 2022, 55, 7663−7673 Read Online

ACCESS | Metrics & More | Article Recommendations | Supporting Information

ABSTRACT: The effect of lignin nanoparticles (LNPs) on the crystallization kinetics of poly(ethylene oxide) (PEO) is examined. Lignin from spruce and ionic isolation was used to prepare LNPs with a number-averaged diameter of 85 nm (with a relatively large polydispersity) by an ultrasonication method. PEO-based nanocomposites with four different LNP contents (5, 10, 15, and 20 wt %) were prepared and subject to isothermal and nonisothermal crystallization protocols in a series of experiments. Scanning electron microscopy (SEM) images showed well-dispersed LNPs in the crystallized PEO matrix. The incorporation of LNPs exponentially increases nucleation density at moderate loadings, with this trend apparently saturating at higher loadings. However, the spherulitic growth rate decreases monotonically with LNP loading. This is attributed to the substantial PEO/LNP affinity, which impacts chain diffusion and induces supernucleation effect (with efficiencies in the order of 200%), but leads to slower growth rates. The overall crystallization kinetics, measured by the DSC, shows faster nanocomposite crystallization rates relative to the neat PEO at all LNP contents examined. This indicates that the supernucleation effect of LNPs dominates over the decrease in the growth rates, although its influence slightly decreases as the LNP content increases. The strong hydrogen-bonded interactions between the LNPs and the PEO are thus reminiscent of confinement effects found in polymer-grafted NP nanocomposites (e.g., PEO-g-SiO_2/PEO) in the brush-controlled regime.

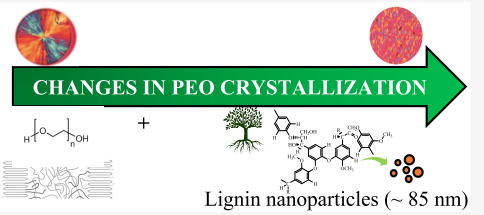

1. INTRODUCTION

Industries have been shifting into sustainable alternatives, and the use of biodegradable/biocompatible materials has been the focus of various groups.[1−4] Poly(ethylene oxide) (PEO) is a biocompatible, semicrystalline polymer used in various applications:[5] solid electrolytes,[6,7] for drug delivery,[8,9] in biomedical scaffolds,[10] and for polymer fabrication.[11,12] An easy way to create robustly advanced materials from such a polymer is through nanoparticle (NP) incorporation.[13,14] Since PEO is a semicrystalline polymer with a high degree of crystallinity, the corresponding nanocomposite and blend properties are highly affected by changes in the crystallization kinetics and the final semicrystalline PEO morphology. Thus, many studies have focused on understanding how NP addition affects crystallization kinetics[15−18]—this topic is precisely the focus of this paper.

Incorporating lignin as a filler is a direct path toward developing economically and sustainably appealing polymer nanocomposites. Lignin is a renewable and naturally available material, considered the second most abundant biomacromolecule (after cellulose).[2,3] Lignin is also relatively inexpensive, biodegradable, and has substantial antioxidant and antibacterial properties.[19] Therefore, the preparation of polymer hybrid materials, with lignin as a filler, has been the scope of several studies.[4,19−23] It was shown that polymer/filler compatibility plays a major role in enhancing the crystallization kinetics of the hybrid,[24,25] where incompatible, phase-separated mixtures always lead to undesired results and deteriorated properties.[26] Although lignin shows unfavorable interactions with most synthetic polymers and natural rubbers, it has good affinity to PEO.[27] Kubo and Kadla[28] have shown that lignin forms strong hydrogen bonds with PEO chains, usually leading to compatible mixtures over a wide range of PEO molecular weights. They have also shown that PEO/lignin mixtures exhibit a single glass-transition temperature (T_g) that increases as the lignin content increases. Such T_g behavior, which presumably resulted from well-dispersed highly interacting lignin NPs, has been confirmed by Wu et al.[19] and others.[29]

This paper compares the nucleation efficiency of LNPs against that achieved by inorganic NPs (e.g., silica); we also examine their effect on decreasing spherulitic growth kinetics. Previous works have shown that inorganic NPs act as nucleating or antinucleating agents based on their dispersion states, surface chemistry, aspect ratio, and loadings.[16,24,25,30−32] That is, well-dispersed and surface-modified NPs can act as

Received: May 4, 2022
Revised: July 7, 2022
Published: August 26, 2022

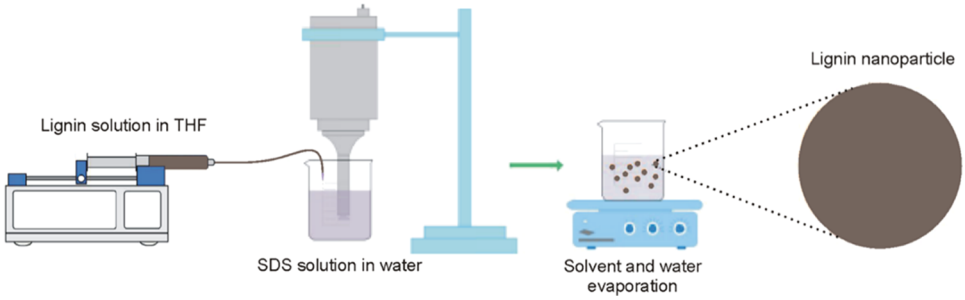

Figure 1. Schematic representation of the experimental procedure for the preparation of lignin nanoparticles (LNP).

heterogeneous nucleation sites that lead to orders of magnitude increase in nucleation efficiency, as confirmed by various studies.[30,33] As aggregation usually occurs upon increasing NP concentration, the nucleation efficiency tends to decrease, resulting in an optimum at moderate loadings.[34] In terms of growth kinetics, the incorporation of spherical NPs usually decreases the spherulite growth rate beyond a specific concentration.[35] The extent of such decrease is mainly affected by NP content (interparticle spacing), surface chemistry, and NP aggregation.[32] Altorbaq et al.[36] have shown that grafted NPs lead to a relatively larger decrease in the spherulitic growth rate compared to observations with bare NPs.

Here, we characterize the LNP dispersion state and its affinity with the PEO matrix through scanning electron microscopy (SEM) and Fourier transform infrared (FTIR), respectively. We then study the effect of LNP content, dispersion state, and surface chemistry on the nucleation and growth kinetics of PEO using polarized light optical microscopy (PLOM). Finally, we evaluate the overall crystallization kinetics in both isothermal and nonisothermal protocols using differential scanning calorimetry (DSC) and enunciate how the nucleation and growth steps separately contribute to the observed overall crystallization kinetics.

2. EXPERIMENTAL SECTION

2.1. Materials. PEO (viscosity average molecular weight, M_v = 100 kDa) was purchased from Sigma-Aldrich (Madrid, Spain). Lignin from spruce and ionic isolation process was used. The isolation method is a patented procedure (DE102010048614A1) that uses imines. The main characteristics of lignin are: ash content = 0.6 wt %, moisture content = 23.34 wt %; C, N, S, H contents = 66.26, 0.26, 0.71, and 8.27%, respectively; molecular weights M_w and M_n = 3718 and 768 Da, respectively.[37] Sodium dodecyl sulfate (SDS, Anedra) and tetrahydrofuran (THF, Cicarelli) were used as received.

2.2. Synthesis of Lignin Nanoparticles. LNPs were prepared using an ultrasonication method, as illustrated in Figure 1. Lignin was first dissolved in THF at a concentration of 0.3% w/v. The solution (15 mL) was then added dropwise into a reactor containing 50 mL of 0.1% w/v SDS aqueous solution using a syringe pump at a flow rate of 5 mL/min. The system was sonicated during the addition using an ultra-sonicator probe (Sonics VC 750) at 75% amplitude with cycles of 15 s on and 5 s off. The aqueous phase was maintained under magnetic stirring during the protocol, and the reactor was equipped with a cooling system. The obtained solution was vacuum dried to collect the LNPs. The particles were redissolved in water and probe-sonicated for further use. SDS has been used as a surfactant to stabilize the lignin NPs (LNPs) upon their decomposition into smaller, nanometer-sized particles, thus preventing subsequent aggregation. Direct measurement of the SDS adhesion on the LNP was complicated due to the small molecular size of SDS. However, obtaining LNPs in the nanometer ranges (see Figure S1) conjectures that these particles have been well stabilized by the SDS; that is, SDS molecules not localized at the interface results in LNP aggregation in the aqueous solution, leading to a micron-sized LNP formation.

2.3. Sample Preparation. Solution mixtures of PEO (5 wt %) and LNPs (1 wt %) in water were first prepared. Different PEO/LNPs weight compositions were mixed: 95/05, 90/10, 85/15, and 80/20. These mixtures were stirred for one hour at room temperature, and then solvent-cast onto silicon molds. The resulting films were dried at room temperature and then under high vacuum at 50 °C for 1 day.

2.4. Dynamic Light Scattering. Dynamic Light Scattering (DLS) was performed using Malvern Instruments (Zetasizer Nano Z) to determine the mean LNP size. The light source is a He−Ne laser with a wavelength and a scattering angle of 633 nm and 173°, respectively. The suspensions were prepared by dispersing the solid powder in ultrapure water at a concentration of about 0.1 g/L, then treated for 6 min in an ultrasonic bath. The measurements were performed at room temperature.

2.5. Fourier Transform Infrared Spectroscopy. FTIR measurements of neat LNP, neat PEO, and PEO/LNP nanocomposites were conducted on a Shimadzu Model 8201 Fourier transform spectrophotometer in the frequency region of 4000−500 cm^{-1} at 40 scans. Potassium bromide (KBr) disks were employed to avoid interferences in the absorbance and obtain higher resolution spectra. The resulting spectra were then processed using Hyper IR software.

2.6. Scanning Electron Microscopy. Scanning electron microscopy (SEM) was performed using Nova NanoSEM 450 (FEI) instrumentation at Columbia University's Clean Room Laboratory. The instrument is equipped with a FEG electron gun that uses an ultra-high brightness Schottky field emitter. The secondary electron mode was used for imaging at an acceleration voltage of 5 kV. The samples were first cryo-fractured, then mounted on a stub using copper tape, and then sputter-coated with Ag/Pd using a Cressington 108 manual sputter coater instrument for one minute to reduce charging (6 nm thick layer).

2.7. Differential Scanning Calorimetry. Calorimetry experiments were performed using a PerkinElmer DSC 8000 instrument equipped with an Intracooler II. The DSC was calibrated with indium and tin standards. Samples of ∼5 mg mass were encapsulated in aluminum pans and sealed. Ultra-high purity nitrogen was used to provide an inert atmosphere. For the nonisothermal analysis, the heating and cooling rates were 20 °C/min. The samples were first heated from 25 to 100 °C, kept for 3 min at 100 °C to erase thermal history, and then cooled to −70 °C; the corresponding cooling scans were recorded. The samples were then heated to register the subsequent heating scans.

For the isothermal crystallization studies, the experiments were carried out following the detailed procedure recommended by Müller et al.[38] Samples were heated to 100 °C at 20 °C/min and kept at that temperature for 3 min to erase any previous history. Then, the samples were cooled at 60 °C/min to the chosen isothermal crystallization temperature (T_c). The T_c range employed for each sample was previously determined by preliminary tests to ensure that no crystallization occurred during the cooling step.

Self-nucleation (SN) measurements were performed according to the Fillon et al. experimental protocol.[39−41] The samples were heated to 120 °C for 3 min to erase thermal history. Then, a standard thermal history was created by cooling the samples at 20 °C/min to

https://doi.org/10.1021/acs.macromol.2c00925
Macromolecules 2022, 55, 7663−7673

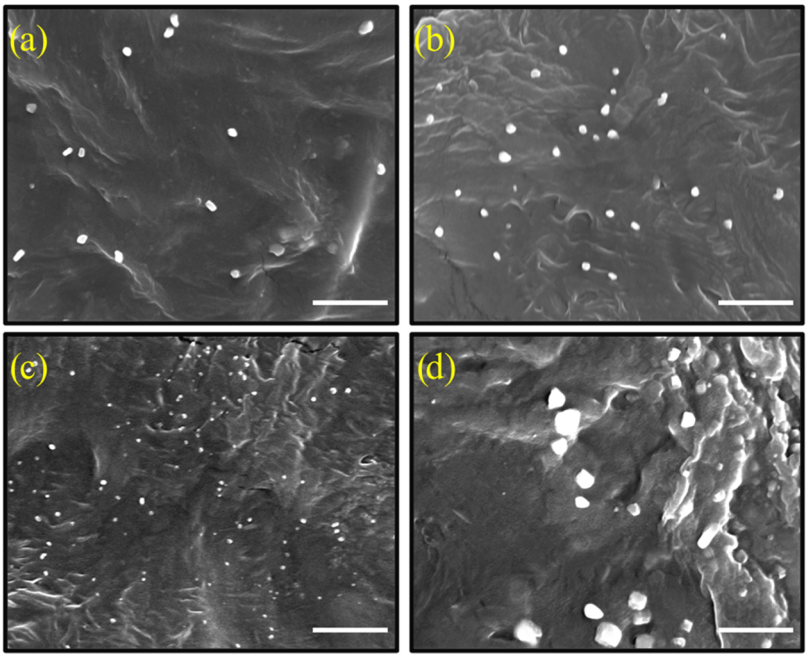

Figure 2. Scanning electron microscopy (SEM) images of the PEO/LNP nanocomposites. PEO/LNP weight ratios are (a) 95/05 and (b–d) 80/20. Scale bars are 1 μm. LNPs appear brighter due to their higher electron density compared to the PEO matrix.

−20 °C. Then they were subsequently heated at 20 °C/min to a temperature denoted as the self-nucleation temperature (T_s). The subsequent cooling scan was then recorded to measure T_c. Finally, the samples were heated to 120 °C to record the final heating scan after SN. These steps were repeated using a wide range of T_s temperatures.

2.8. Polarized Light Optical Microscopy. Nucleation and growth measurements were conducted using an Olympus BX51 polarized light optical microscope (PLOM) equipped with an SC50 digital camera. A Linkam (THMS600) stage was used for accurate temperature control with an accuracy of 0.1 °C. The samples were first melted at 100 °C for 3 min, then cooled down to the required isothermal temperature at 50 °C/min. The nucleation density and spherulite size were determined using ImageJ analysis package.[42] The spherulitic growth rate was calculated from the slope of spherulite radius versus time plots, which were always linear.

3. RESULTS AND DISCUSSION

3.1. LNP Dispersion and Compatibility. The LNP size and its distribution are discussed in the Supporting Information (DLS measurements and TEM and AFM images of LNPs). Figure S1 shows that the size distribution of LNPs is broad; such a high dispersity is intrinsic to the sonication method employed here. For more details on the LNP synthesis, the reader is referred to the published works;[37,43] here, we focus mainly on the LNP/PEO dispersion state and crystallization kinetics.

Figure 2a,b shows the LNP dispersion states as characterized by SEM at loadings of 5 and 20 wt %, respectively. Regardless of loading, the LNPs are well dispersed in the PEO matrix, except for some slight aggregation observed in certain areas of the sample with 20 wt % LNPs (see Figure 2d). (Figure 2b–d shows LNP dispersion states in different regions of the same sample with the highest loading.) The good dispersion is likely due to the favorable hydrogen bond interaction between the PEO and LNP. This is in good agreement with the works of Wu et al.,[19] and Kubo and Kadla,[28] who have shown that the PEO and lignin are compatible and hence well dispersed over the entire compositional range. FTIR evidence for hydrogen bonding between the nanocomposite's components is provided below.

Figure 3a shows FTIR spectra separately for the neat PEO and LNP. For the pristine LNPs (dashed-curve), characteristic bands observed in the range of 600–3900 cm^{-1} correspond to −OH stretching—3700–3100 cm^{-1} (L1), alkyl stretching—2921 cm^{-1} (L2), aromatic C=C stretching—1519 cm^{-1} (L3), phenolic −OH bending—1463 cm^{-1} (L4), aromatic skeleton—1600 cm^{-1} (L5), C−O−C stretching—1224 (L6) and 1083 (L7) cm^{-1}. In the case of neat PEO (solid curve), the characteristic bands correspond to aliphatic −CH stretching—2879 cm^{-1} (P1), −CH bending—1467 cm^{-1} (P2), C−O−C (symmetric and asymmetric) stretching- 1096 cm^{-1} (P3), and CH_2 rocking vibration—836 cm^{-1} (P4). Note that the −OH band from lignin is more intense than the corresponding band from the PEO due to the multiple OH groups in the lignin structure.

The FTIR spectra of polymer nanocomposites (with LNP contents of 10, 15, and 20 wt %), shown in Figure 3b, are compared to the neat PEO and the pristine LNP to confirm the molecular interactions between the mixture components. Upon the incorporation of LNPs into the PEO matrix, the characteristic broadband of OH groups (3700–3100 cm^{-1}) in the LNP is slightly shifted to lower wavenumbers. Additionally, the intensity of the aromatic skeleton characteristic band at 1600 cm^{-1} (LP2) of the composites increases with LNP contents (i.e., 10 vs 20 wt %). Previous work[29] attributed the shift of the characteristic band of −OH groups to the formation of intermolecular hydrogen bonds, and it is in good agreement with our results. In addition, the −OH band was deconvoluted into two peaks corresponding to hydrogen-bonded −OH and free OH, and the results are presented in the Supporting information (Figure S2).

3.2. Effect of LNP on PEO Nucleation Kinetics. PLOM is employed to measure the nucleation density (ρ_{nuclei}) of PEO/LNP nanocomposites according to the experimental procedure discussed in Section 2.8. Figure 4 plots ρ_{nuclei} vs time

https://doi.org/10.1021/acs.macromol.2c00925
Macromolecules 2022, 55, 7663−7673

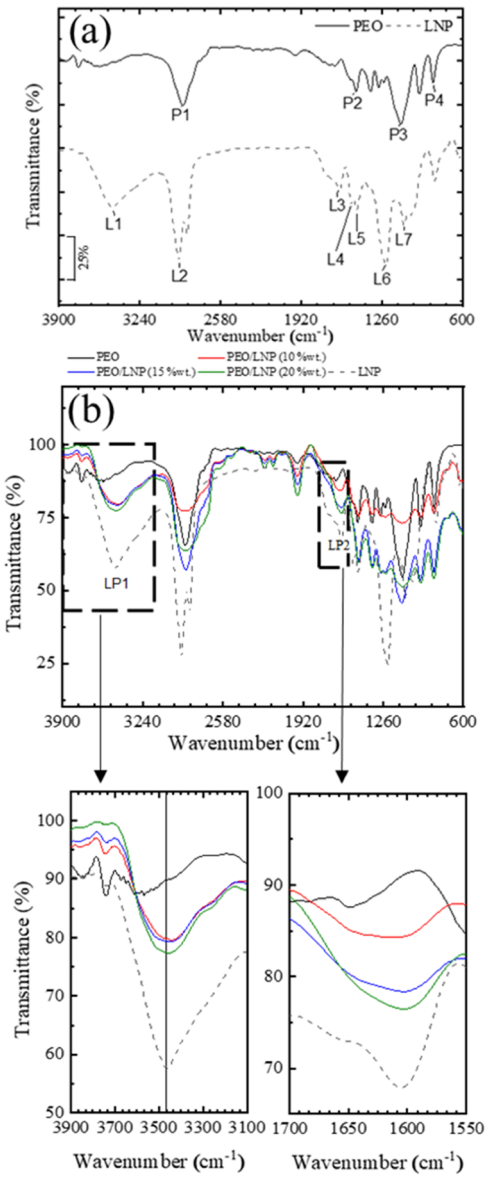

Figure 3. (a) Fourier transform infrared (FTIR) spectra for the neat PEO and LNPs. Curves are offset along the *y*-axis for clarity. (b) FTIR spectra for neat LNPs, neat PEO, and PEO/LNP nanocomposites (with LNP contents of 10, 15, and 20 wt %). The bottom row shows higher magnifications of the labeled regions in (b).

for the neat PEO (a) and nanocomposites (b–d) over a wide range of T_c values.

As expected, for all samples the primary nucleation density increases as the crystallization temperature decreases. Notably, the incorporation of LNP leads to an order of magnitude increase in ρ_{nuclei} implying that LNPs act as heterogeneous primary nucleating sites during isothermal crystallization. Such a significant enhancement in the primary nucleation kinetics is attributed to good LNP dispersion and favorable LNP/PEO interactions. These results are in accordance with the literature.[30,33] Wen et al.[30] showed in the case of PEO/SiO_2 nanocomposites that the surface modification of the silica with PEO leads to good dispersion and, therefore, to a similar enhancement in the PEO nucleation kinetics. They have also shown that the unmodified silica leads to an aggregated morphology that results in antinucleation effects.

To get a direct measure of the primary nucleation kinetics, we evaluate the nucleation rate (I) of the nanocomposites (Figure 5) by taking the time-derivative of ρ_{nuclei} at short times where the dependence is linear ($I = \partial\rho_{nuclei}/\partial t$). The Turnbull–Fisher (TF) model[44−46] is used to describe the experimental data in Figure 5

$$\log I = \log I_O - \frac{\Delta F^*}{2.3kT} - \frac{16\sigma\sigma_e(\Delta\sigma)T_m^{o2}}{2.3kT(\Delta T)^2(\Delta H_v)^2} \quad (1)$$

where I_O represents contributions from the diffusion of polymer segments to the nucleation site, k is the Boltzmann constant, ΔF^* is a parameter related to the primary nucleation free energy, σ_e and σ are, respectively, the fold and lateral surface free energies, ΔH_v is the volumetric melting enthalpy ($\Delta H_v = \Delta H_m^0 \cdot \rho$), ΔH_m^0 is the melting enthalpy of 100% crystalline PEO (214 J/g),[47] and ρ is the PEO density (1.13 g/cm^3, reported by the manufacturer). ΔT is the undercooling (i.e., $\Delta T = T_m^o - T_c$), where T_m^o is the equilibrium melting temperature (T_m^o = 79 °C).[48] The detailed procedure of parameter evaluation is presented in the Supporting Information (see Table S2). The melt-nucleus interfacial free energy difference ($\Delta\sigma$) is then determined from the TF fit in Figure 5 (i.e., $\Delta\sigma$ is proportional to the slope).

Figure 6 plots $\Delta\sigma$, a measure of the free energy difference between the heterogeneous nucleus and the melt, as a function of LNP content. Clearly, the incorporation of LNP leads to an unexpected decrease in $\Delta\sigma$ as a function of LNP content, with the results effectively flattening out to within uncertainties at larger NP loadings. Thus, a lower free energy difference caused by the incorporation of LNP suggests more stable nucleus formation, leading to higher nucleation density even at temperatures elevated compared to neat PEO. Such a decrease in $\Delta\sigma$ has been linked to higher nucleation efficiencies.[34,44,49] Furthermore, the saturation of the nucleation at 15% could be an indication that NP aggregation sets in; the "larger" NPs observed in Figure 2d at 20% loading are consistent with this interpretation. The trend reported in Figure 6 is also consistent with the nucleation efficiency of the LNPs, as we will discuss below (see Figure 11 and its discussion).

3.3. Effect of LNP on PEO Growth Kinetics. PLOM measurements are conducted to delineate the effect of LNPs on the PEO spherulitic growth rate (G). Figure 7a,b summarizes changes in G and relative growth rate (G/G_{PEO}), respectively, for the different LNP content as a function of isothermal crystallization temperature. Figure 7a shows that LNPs reduce the experimentally determined spherulitic growth rates when crystallizing at similar T_cs. Such a decrease in the growth kinetics is presumably due to the PEO/LNP interactions which affect the diffusion of the chains to the growth front.

The Lauritzen–Hoffman (LH) model[50,51] is used to fit the spherulitic growth rates (solid lines in Figure 7a)

$$G = G_0 \exp\left(\frac{-U^*}{R(T - T_\infty)}\right)\exp\left(\frac{-K_g^G}{fT\Delta T}\right) \quad (2)$$

where G_0 is a preexponential growth rate constant, U^* is the transport activation energy of the polymer chain (commonly taken as 1500 cal/mol [6280 J/mol]), K_g^G is a parameter proportional to the secondary nucleation activation energy, R is the universal gas constant (8.134 J·mol^{-1}·K^{-1}), T_∞ is the temperature at which chain dynamics ceases (=T_g − 30), and f

https://doi.org/10.1021/acs.macromol.2c00925
Macromolecules 2022, 55, 7663−7673

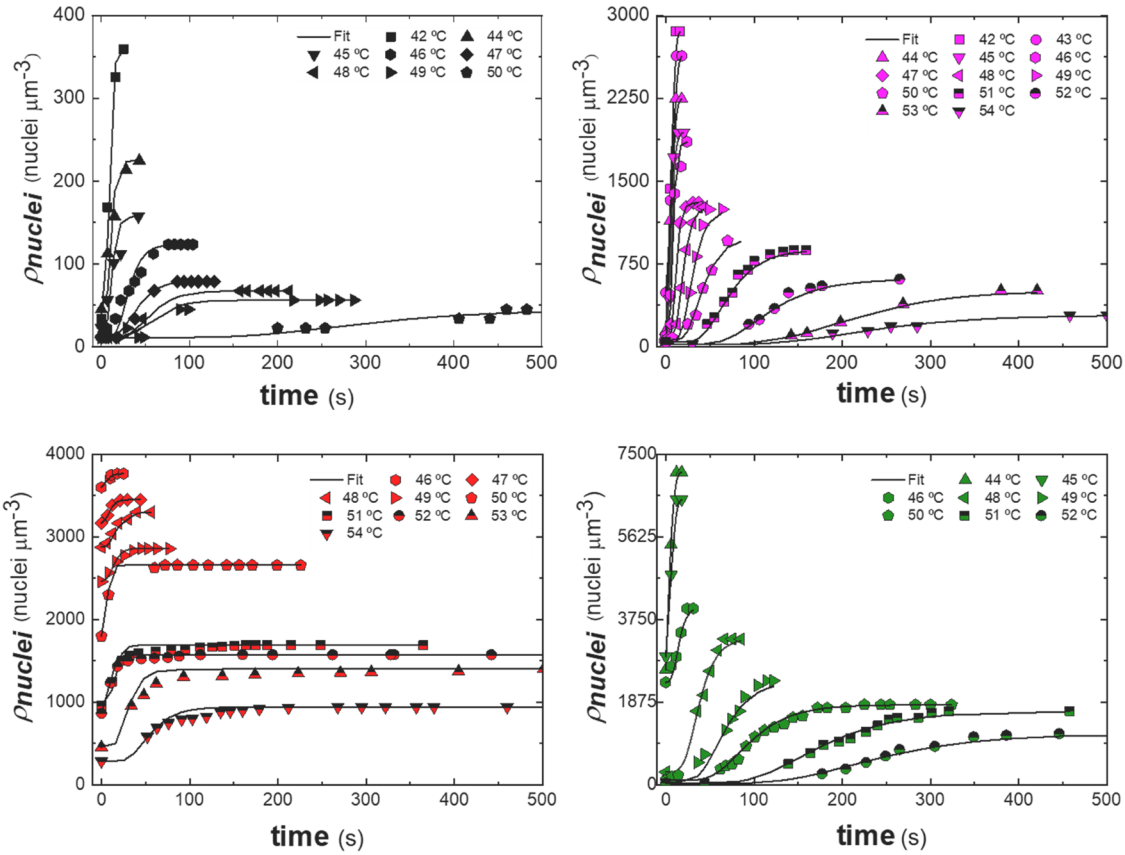

Figure 4. Nucleation density (ρ_{nuclei}) plotted as a function of time at various crystallization temperatures for (a) neat PEO, (b) PEO/LNP:95/05, (c) PEO/LNP:90/10, and (d) PEO/LNP:80/20. The lines through the data points are a guide to the eye.

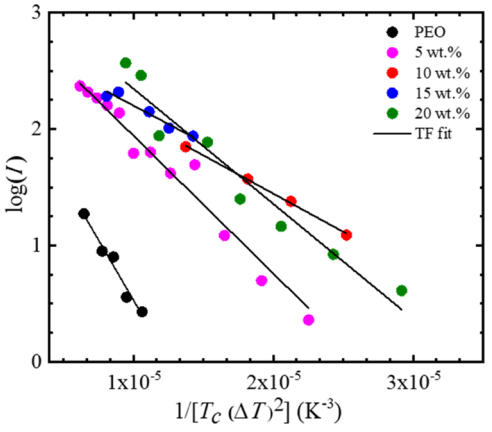

Figure 5. Plot of the nucleation rate (I) vs $1/(T_c\ \Delta T)^2$ for the different LNP loadings. Solid lines correspond to Turnbull−Fisher (TF) fits.

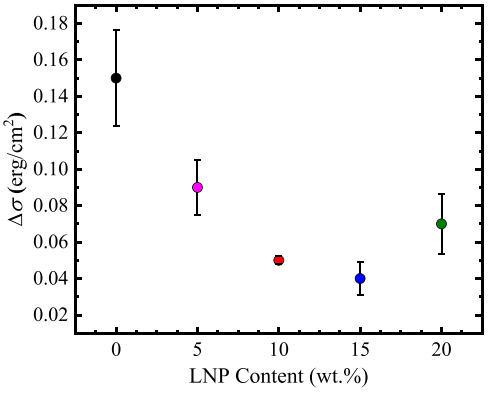

Figure 6. Free energy difference ($\Delta\sigma$) plotted as a function of LNP content.

is a temperature correction factor ($f = 2T_c/(T_m^0 + T_c)$). The first exponential in eq 2 is related to the diffusion of the polymeric chains from the melt to the crystal front. The second exponent describes the energetic contribution for polymeric chains to form secondary nuclei on the growth front. Thus, the growth can be modeled as the product of two contributions: (i) chain diffusion and (ii) secondary nucleation activation energy.

It is clear from Figure 7 that the incorporation of an increased amount of LNP leads to a further reduction in the growth kinetics of the nanocomposites. While G is a strong function of temperature (Figure 7a), G/G_{PEO} is essentially temperature-independent (Figure 7b). This leads to K_g^G values that are unaffected by the presence of the LNPs ($K_g^G/K_{gPEO}^G \approx 1$, Figure 8). Thus, LNPs suppress growth kinetics by slowing down the polymeric chain diffusion in the melt (i.e., the first term in the LH model, $G_0 \exp\left(\frac{-U^*}{R(T-T_\infty)}\right)$), while the secondary nucleation mechanism (K_g^G) is unaffected. These results are in good agreement with previous studies performed on PEO/SiO_2,[35] PEO/PMMA-g-SiO_2,[36] and PE/PE-g-SiO_2[52] systems. Altorbaq et al.[36] associated the reduction in the growth kinetics due to the increase in the nanocomposite melt viscosity (η) upon the addition of NPs. It was shown that the chain

https://doi.org/10.1021/acs.macromol.2c00925
Macromolecules 2022, 55, 7663−7673

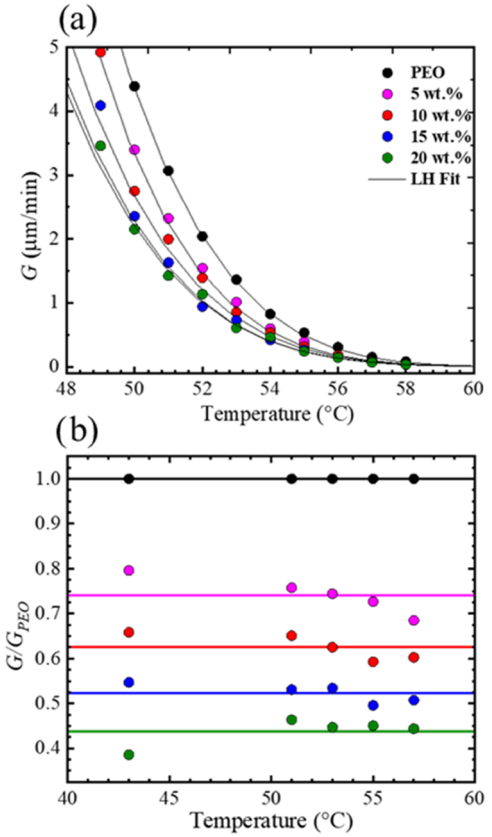

Figure 7. (a) Growth rate (G) plotted for each LNP loading. Solid lines correspond to Lauritzen–Hoffman (LH) fits. (b) Nanocomposite growth rate normalized by the neat PEO (G/G_{PEO}) at each measured temperature. Solid lines correspond to G/G_{PEO} values averaged over all temperatures, showing how G/G_{PEO} (solid symbols) are scattered away from the corresponding averaged value.

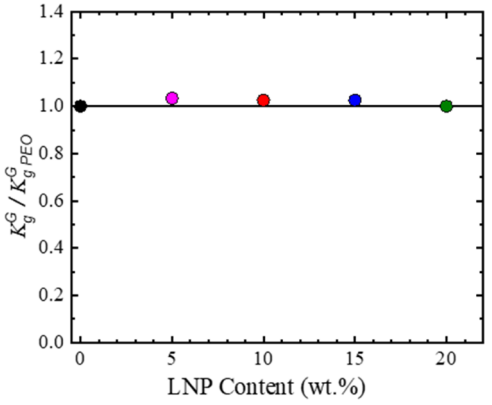

Figure 8. Relative change in the secondary nucleation activation energy parameter (K_g^G/K_{gPEO}^G) plotted as a function of LNP content.

diffusion term in the LH model can be related to η^{-1} through the Vogel–Fulcher–Tammann equation;[53−55] thus, $G/G_{PEO} = \eta_{PEO}/\eta$. They confirmed this behavior using small amplitude oscillatory shear measurements. As similar results are obtained with PEO/LNP nanocomposites, we thus attribute the observed reduction in spherulitic growth for the PEO/LNP nanocomposite to an increase in PEO melt viscosity—indeed, recent studies have shown that the incorporation of lignin leads to a significant viscosity increase.[19]

In the latest revisions of the original Lauritzen and Hoffman crystallization theory performed by Hoffman et al.,[56,57] they incorporated the reptation dynamics of macromolecules in an isotropic entangled melt and postulated that the preexponential factor G_0 is a function of the inverse of the number of segments within the polymer chain (n). Hence, while U^* could be considered proportional to the local chain segmental mobility at the growth front, G_0 values depend on the reptation of the entire chain, which is a function of melt viscosity. In the results presented in this section, we show that LNP addition does not influence the local segmental dynamics during secondary nucleation at the growth front, as U^* remains constant. However, lignin-PEO interactions slow down the reptation of the polymer chains with a concomitant melt viscosity increase. In conclusion, the decrease in PEO spherulitic growth rate observed with increasing LNP concentration (Figure 7) can be interpreted as being caused by the slowing down of the global chain dynamics due to PEO-lignin interactions (detected by FTIR in Figure 3).

The extent of confinement imposed by the LNPs can be quantified using different metrics.[35,58] In this context, we use the ratio of the LNP surface area (SA_{LNP}) to the PEO volume (V_{PEO}) adopted from Jimenez et al.[35] It was shown that SA_{LNP}/V_{PEO} is an accurate measure of the confinement in each of the PEO/SiO_2,[35] PEO/PMMA-g-SiO_2,[36] and PE/PE-g-SiO_2[52] systems. For comparison, we replot $G/G_{polymer}$ of the previously published systems, and superimpose the average G/G_{PEO} values of the PEO/LNP nanocomposites as a function of confinement (Figure 9). (For detailed measurements of SA_{LNP}/V_{PEO}, see the Supporting Information.)

Two distinct regimes were observed by Altorbaq et al.[32,36] as shown in Figure 9: (i) NP-dominated and (ii) brush-controlled regimes. In the brush-controlled regime, growth kinetics are

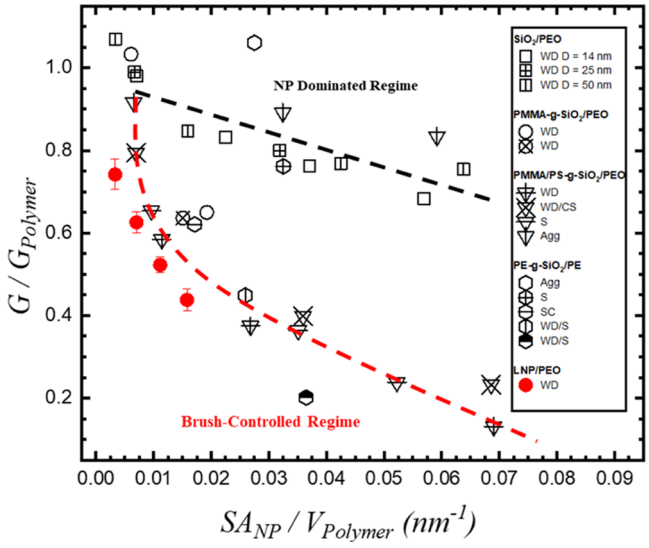

Figure 9. Relative growth rate change ($G/G_{Polymer}$) replotted as a function of confinement ($SA_{NP}/V_{Polymer}$) for each of PEO/SiO_2,[35] PEO/PMMA-g-SiO_2,[36] and PE/PE-g-SiO_2[52] systems. G/G_{PEO} values for PEO/LNP composite, taken from the averaged values in Figure 7b (solid lines), are superimposed for comparison (red solid circles). Dashed lines correspond to the two general observed regimes: NP-dominated regime (black curve) and brush-controlled regime (red curve). The NP dispersion states of the reported works are shown in the legend as well-dispersed (WD), connected-sheets (CS), strings (S), and aggregated (Agg) structures.[32]

https://doi.org/10.1021/acs.macromol.2c00925
Macromolecules 2022, 55, 7663−7673

highly suppressed by the chemically bonded chains on the NP, resulting in a strong growth reduction (Figure 9, red curve). Bare and aggregated grafted NPs show a much weaker effect on the growth kinetics denoted as NP-dominated regime (Figure 9, black curve). Clearly, LNPs strongly decrease the growth rate of the PEO, closely tracking the behavior observed in the brush-controlled regime in Figure 9. We ascribe this result to the (strong) hydrogen bonds between the well-dispersed LNPs and the PEO matrix.

3.4. Overall Crystallization Kinetics and Self-Nucleation. *3.4.1. Nonisothermal Crystallization.* DSC experiments have been performed to understand the effect of LNPs on overall PEO crystallization kinetics (nucleation and growth). First, we performed nonisothermal crystallization measurements using the heat-cool-heat protocol (see Section 2.7) to evaluate each of the nonisothermal crystallization parameters: T_c, T_m, and χ_c (the degree of crystallinity). Figure 10 plots both

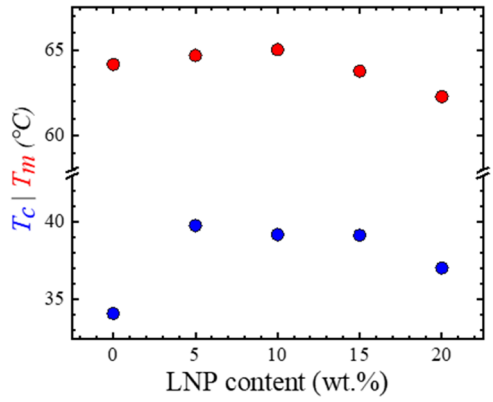

Figure 10. Nonisothermal DSC results showing peak values of the crystallization temperature, T_c (blue), and melting temperature, T_m (red), as a function of LNP content.

T_c (blue) and T_m (red) peak values as a function of LNP content. (DSC scans and χ_c values are shown in the Supporting Information, see Figure S5 and Table S4). The nanocomposite melting behavior (i.e., T_m) shows minimal changes relative to the neat PEO. This indicates that the crystalline lamellar thickness is only slightly affected by the LNPs.

Further, nonisothermal crystallization kinetics are enhanced by LNP addition; this is manifest by a 6 °C increase in the T_c values upon the addition of LNPs. Such enhancement is due to an increase in nucleation kinetics. At 20 wt % LNP content, the decrease in interfacial contacts and dispersion quality start to suppress nucleation. The observed enhancement in the crystallization kinetics and the following decrease upon further LNP incorporation are in good agreement with various nanocomposite systems: one-dimensional carbon nanotubes,[59,60] two-dimensional graphene sheets[61] and clays,[34] and three-dimensional, spherical NPs.[30]

Next, we evaluate the nucleation efficiency (*NE*) for the different LNP contents following the Fillon et al. protocol[39,41]

$$\%NE = \frac{T_c^{LNP} - T_c^{PEO}}{T_c^{max} - T_c^{PEO}} \times 100 \quad (3)$$

where T_c^{LNP} and T_c^{PEO} are the nanocomposite and neat PEO crystallization temperatures measured from nonisothermal DSC experiments, respectively, and T_c^{max} is the maximum crystallization temperature of neat PEO determined at the lowest T_s of *Domain II* (see the Supporting Information for more details). Based on *NE* values, the noncrystallizable components can be characterized as: nucleating (*NE* = 0–100%), supernucleating (*NE* > 100%), or antinucleating (*NE* <0%) agents.[32]

Figure 11 plots *NE* as a function of LNP content. LNPs are remarkably supernucleating agents for PEO. Notice that in

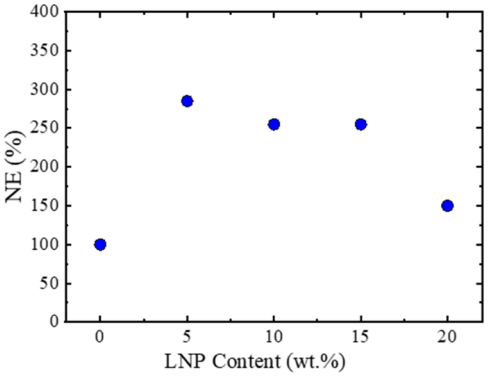

Figure 11. Nucleation efficiency (*NE*) plotted as a function of LNP content.

Figure 11, the value reported for neat PEO corresponds to that of the ideally self-nucleated sample, and hence a value of 100% *NE* is reported, as in that case T_c^{LNP} must be substituted by T_c^{max} in eq 3. Once again, aggregation limits supernucleation for an LNP concentration of 20 wt %. Previous works have shown that carbon nanotubes can also be supernucleating agents for PEO, PE, and PCL.[16,17] This means that the nucleating action of these nanofillers, and in the present case LNPs, can be more efficient than the polymer's own self-nuclei in triggering heterogeneous nucleation. These results are in very good agreement with nucleation kinetics measured under isothermal conditions (see Figure 6 and compare with Figure 11).

One point to address is that most of the reported nucleating agents have been discussed in terms of nucleation efficiency, where the exact mechanism has not yet been clearly understood. In other NP systems (such as SiO_2, graphene sheets, clays),[32] it has been shown that well-dispersed NPs (with favorable NP–polymer interaction) result in better nucleation power, where aggregated structures lead to low *NE* values. Herein, despite the nucleation mechanism, we show that organic LNPs outperformed commercially available inorganic nucleating agents, providing a renewable, biocompatible replacement.

3.4.2. Overall Isothermal Crystallization Kinetics. Previous works demonstrated that the observed isothermal overall crystallization kinetics (using the DSC) could be dominated by nucleation kinetics in many cases,[33,49,62] or sometimes by growth.[48] We perform isothermal DSC measurements to understand the contribution of nucleation and growth processes to overall crystallization kinetics. Isothermal exotherms were recorded according to the experimental procedure discussed in Section 2.7. The overall crystallization rates are then estimated by calculating the inverse of the half-crystallization time ($1/\tau_{50\%}$).

Figure 12a,b compares the corresponding $1/\tau_{50\%}$ and $[1/\tau_{50\%}]/[1/\tau_{50\%,PEO}]$ as a function of isothermal crystallization temperature. For comparison, the averaged $[1/\tau_{50\%}]/[1/$

https://doi.org/10.1021/acs.macromol.2c00925
Macromolecules 2022, 55, 7663–7673

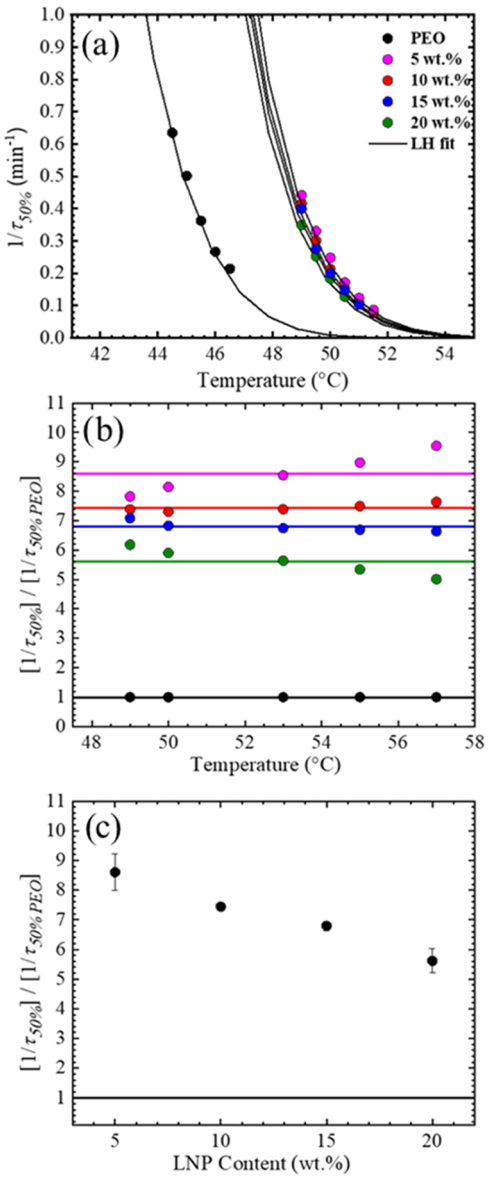

Figure 12. (a) Overall crystallization rate $1/\tau_{50\%}$ and (b) the corresponding normalized rate $[1/\tau_{50\%}]/[1/\tau_{50\%,PEO}]$ plotted as a function of temperature for different LNP loadings. Solid lines correspond to (a) LH fits and (b) $[1/\tau_{50\%}]/[1/\tau_{50\%,PEO}]$ averaged values. (c) $[1/\tau_{50\%}]/[1/\tau_{50\%,PEO}]$ averaged values plotted as a function of LNP content.

$\tau_{50\%,PEO}]$ values across the measured temperatures (solid line in Figure 12b) are plotted as a function of LNP content (Figure 12c).

Clearly, the incorporation of LNP always leads to an overall crystallization enhancement ($1/\tau_{50\%} > 1/\tau_{50\%,PEO}$), Figure 12a. This is attributed to the dominant effect of nucleation (which is very strong in this particular case, i.e., LNP are supernucleating agents) over growth (since G/G_{PEO} is always lower than unity). Figure 12 shows an order of magnitude increase in $[1/\tau_{50\%}]/[1/\tau_{50\%,PEO}]$ for the lowest loading, which is in good agreement with the nucleation kinetics measured with the PLOM. However, as we further increase the LNP content, $1/\tau_{50\%}$ starts to decrease monotonically. This is ascribed to the stronger suppression in the growth imposed by the increasing amount of the well-dispersed LNPs. The LH model (eq 2) applied to the isothermal DSC data is used to evaluate K_g^τ, a parameter proportional to the primary and secondary nucleation activation energy (denoted with a superscript τ and is related to both nucleation and growth). Although the extent of enhancement in the overall crystallization rate is dominated by nucleation, $[1/\tau_{50\%}]/[1/\tau_{50\%,PEO}]$ is temperature-independent tracking the behavior of G/G_{PEO} in Figure 7b. Previous works[16,34,49,62] have observed a decrease in K_g^τ upon nucleating agents' incorporation similar to the observed $\Delta\sigma$ trend in Figure 6. This could be attributed to the minimal changes in growth ($G/G_{matrix} \sim 1$) for each of the previously studied systems.

In the present case, the values of K_g^G and K_g^τ (reported in the SI) do not significantly vary with filler loading (see Figure 8 and Figure 13). It is possible that the supernucleation effect is

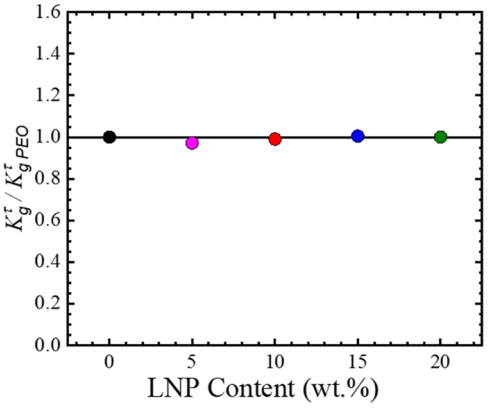

Figure 13. Relative change in the primary plus secondary nucleation activation energy parameter (K_g^τ/K_{gPEO}^τ) plotted as a function of LNP contents.

compensated by the strong polymer/filler interactions that cause reductions in growth rates (see associated confinement effects in G reported in Figure 9), leading to such filler-content-independent values of secondary nucleation and overall crystallization energy barriers. It should be noted that all of the constant K_g^G values can be approximated as 1.2×10^5 K^2, while those of K_g^τ can be approximated to 2.2×10^5 K^2; as expected, the overall crystallization energy barrier is larger by a factor of 2 when the primary nucleation is taken into account together with the growth or secondary nucleation contribution.[63]

To further understand the crystallization process of the PEO/LNP nanocomposites, we fit the experimental data using the Avrami model[64]

$$1 - V_c(t - t_0) = \exp(-k(t - t_0)^n) \quad (4)$$

where t is the crystallization time, t_0 is the induction time, V_c is the relative volumetric fraction transformed (crystallized), k is the overall crystallization rate constant, and n is the Avrami index. (Detailed analysis of the Avrami fit is shown in the Supporting Information, Figure S7.) Müller et al.[65] considered n as the sum of two contributions:

$$n = n_n + n_{gd} \quad (5)$$

where n_n is the nucleation contribution (instantaneous and sporadic nucleation correspond to n_n values of 0 and 1, respectively) and n_{gd} is the growth dimensionality (usually considered in the range of 1−3, where most unconfined polymers grow into spherulites [3D] or axialites [2D]

https://doi.org/10.1021/acs.macromol.2c00925
Macromolecules 2022, 55, 7663−7673

formation). The overall crystallization rate constant k has units of min^{-n}. For comparison across different n values, $k^{1/n}$ (min^{-1}) is then plotted as a function of temperature (Figure 14a), which tracks well with the experimental $1/\tau_{50\%}$ data.

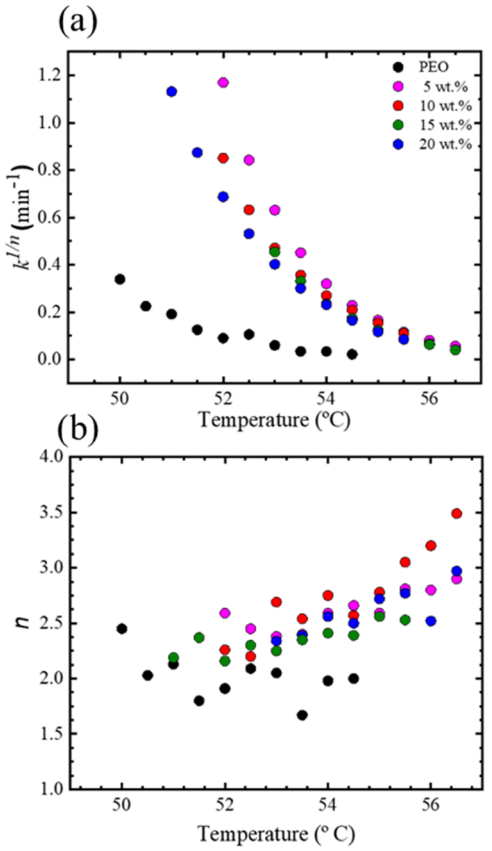

Figure 14. Avrami fit values of $k^{1/n}$ (a) and n (b) plotted as a function of temperature for different LNP contents.

Figure 14b compares n values for each nanocomposite loading. Clearly, LNP is no significant confinement effect on the overall crystallization process (which includes the competing effects of both nucleation and growth), with n values greater than 1.5, at least in the composition range employed here (up to 20% loading). This is unlike behaviors observed in nanotube- and sheet-polymer nanocomposites,[66] which result in n values approaching unity but at much higher nanofiller contents. Our results are in good agreement with studies performed on PEO/SiO_2,[67] showing unconfined crystals with n values in the range of ~3 (2.5 can be approximated to 3)—a value corresponding to instantaneously nucleated spherulites or sporadically nucleated axialites. At higher isothermal crystallization temperatures, Figure 14b shows an increase in n values for the nanocomposite ($n \rightarrow 3.5$). This is related to the occurrence of sporadic nucleation of spherulites when isothermally crystallizing at higher T_c. Similar trends have been observed in previous studies.[34]

4. CONCLUSIONS

We thoroughly investigated the crystallization kinetics of PEO/LNP nanocomposites by first morphologically characterizing the dispersion state of LNP in the PEO matrix, then by quantifying the reduction in the growth rate and separately the enhancement in nucleation kinetics. It was found that LNPs tend to disperse well in the PEO matrix, with slight aggregation occurring at larger LNP contents. Such good dispersion is likely related to the strong multiple hydrogen bonds formed between the LNP and PEO, which was confirmed by FTIR measurements. The former argument can also justify the order of magnitude increase in nucleation rates, with supernucleating efficiencies at moderate LNP contents, which tracks the general behavior observed previously for well-dispersed, surface-modified, inorganic NPs. Compared to bare silica NPs, LNPs show a much stronger reduction in the spherulitic growth rate, following a similar trend previously observed for polymer-grafted NP-based nanocomposites. Finally, the overall crystallization kinetics shows similar trends to the nucleation results when measured at very low LNP content. As we further incorporate LNP, the overall kinetics keeps decreasing since the growth kinetics becomes more depressed at higher LNP content. This elucidates the importance of separately measuring each of the growth and nucleation kinetics, where the DSC measurement is a convolution of both kinetics.

■ ASSOCIATED CONTENT

Supporting Information

The Supporting Information is available free of charge at https://pubs.acs.org/doi/10.1021/acs.macromol.2c00925.

LNP characterization using DLS, AFM, and TEM; deconvolution of the OH band from FTIR analysis;Lauritzen−Hoffman and Turnbull−Fisher parameters evaluation; heating and cooling DSC scans; self-nucleation domains; and Avrami fit (PDF)

■ AUTHOR INFORMATION

Corresponding Authors

Sanat K. Kumar − *Department of Chemical Engineering, Columbia University, New York, New York 10027, United States;* orcid.org/0000-0002-6690-2221; Email: sk2794@columbia.edu

Alejandro J. Müller − *POLYMAT and Department of Polymers and Advanced Materials: Physics, Chemistry and Technology, Faculty of Chemistry, University of the Basque Country UPV/EHU, 20018 Donostia-San Sebastián, Spain; IKERBASQUE, Basque Foundation for Science, 48009 Bilbao, Spain;* orcid.org/0000-0001-7009-7715; Email: alejandrojesus.muller@ehu.es

Authors

María E. Taverna − *INTEC (UNL-CONICET), 3000 Santa Fe, Argentina; UTN Regional San Francisco, 2400 San Francisco, Córdoba, Argentina*

Abdullah S. Altorbaq − *Department of Chemical Engineering, Columbia University, New York, New York 10027, United States;* orcid.org/0000-0002-8069-1790

Jorge L. Olmedo-Martínez − *POLYMAT and Department of Polymers and Advanced Materials: Physics, Chemistry and Technology, Faculty of Chemistry, University of the Basque Country UPV/EHU, 20018 Donostia-San Sebastián, Spain*

Carlos A. Busatto − *INTEC (UNL-CONICET), 3000 Santa Fe, Argentina*

Manuela Zubitur − *Chemical and Environmental Engineering Department, Polytechnic School, University of the Basque Country UPV/EHU, 20018 Donostia-San Sebastián, Spain*

Agurtzane Mugica − *POLYMAT and Department of Polymers and Advanced Materials: Physics, Chemistry and*

https://doi.org/10.1021/acs.macromol.2c00925
Macromolecules 2022, 55, 7663−7673

Technology, Faculty of Chemistry, University of the Basque Country UPV/EHU, 20018 Donostia-San Sebastián, Spain

Verónica V. Nicolau − *UTN Regional San Francisco, 2400 San Francisco, Córdoba, Argentina; Consejo Nacional de Investigaciones Científicas y Técnicas (CONICET), Godoy Cruz 2290 CABA, Argentina*

Diana A. Estenoz − *INTEC (UNL-CONICET), 3000 Santa Fe, Argentina*

Complete contact information is available at: https://pubs.acs.org/10.1021/acs.macromol.2c00925

Author Contributions

The manuscript was written through the contributions of all authors. All authors have given approval to the final version of the manuscript.

Notes

The authors declare no competing financial interest.

■ ACKNOWLEDGMENTS

This work received funding from the Basque Government through grant IT1503−22. S.K.K. acknowledges funding by the U.S. Department of Energy, Office of Science, grants DE-SC0018182, DE-SC0018135, and DE-SC0018111. The authors acknowledged the financial support of Fundación Losano, PIP2011 848, and PUE No. 22920160100007 (CONICET). The authors acknowledge the support of Ana Martínez Amesti, Microscopy: Polymer Characterization Research Service, SGIker (UPV/EHU).

■ REFERENCES

(1) Hu, T. Q.*Chemical Modification, Properties, and Usage of Lignin*; Springer: US, 2012.

(2) Calvo-Flores, F. G. Lignin: A Renewable Raw Material. *Encycl. Renewable Sustainable Mater.* **2020**, *5*, 102−118.

(3) Feldman, D. Lignin Nanocomposites. *J. Macromol. Sci., Part A: Pure Appl. Chem.* **2016**, *53*, 382−387.

(4) Mohanty, A. K.; Vivekanandhan, S.; Pin, J. M.; Misra, M. Composites from Renewable and Sustainable Resources: Challenges and Innovations. *Science* **2018**, *362*, 536−542.

(5) BAILEY, F. E.; KOLESKE, J. V.Chapter 8 - COMMERCIAL APPLICATIONS FOR POLY(ETHYLENE OXIDE). In *Poly (ethylene Oxide)*, BAILEY, F. E.; KOLESKE, J. V., Eds.; Academic Press, 1976; pp 163−169 DOI: 10.1016/B978-0-12-073250-0.50012-X.

(6) Manthiram, A.; Yu, X.; Wang, S. Lithium Battery Chemistries Enabled by Solid-State Electrolytes. *Nat. Rev. Mater.* **2017**, *2*, No. 16103.

(7) Xue, Z.; He, D.; Xie, X. Poly(Ethylene Oxide)-Based Electrolytes for Lithium-Ion Batteries. *J. Mater. Chem. A* **2015**, *3*, 19218−19253.

(8) Aliabadi, H. M.; Lavasanifar, A. Polymeric Micelles for Drug Delivery. *Expert Opin. Drug Delivery* **2006**, *3*, 139−162.

(9) Gillies, E. R.; Fréchet, J. M. J. Designing Macromolecules for Therapeutic Applications: Polyester Dendrimer-Poly(Ethylene Oxide) "Bow-Tie" Hybrids with Tunable Molecular Weight and Architecture. *J. Am. Chem. Soc.* **2002**, *124*, 14137−14146.

(10) Peppas, N. A.; Hilt, J. Z.; Khademhosseini, A.; Langer, R. Hydrogels in Biology and Medicine: From Molecular Principles to Bionanotechnology. *Adv. Mater.* **2006**, *18*, 1345−1360.

(11) Lee, S.; Spencer, N. D. Aqueous Lubrication of Polymers: Influence of Surface Modification. *Tribol. Int.* **2005**, *38*, 922−930.

(12) Li, L.; Chen, N.; Wang, Q. Effect of Poly(Ethylene Oxide) on the Structure and Properties of Poly(Vinyl Alcohol). *J. Polym. Sci., Part B: Polym. Phys.* **2010**, *48*, 1946−1954.

(13) Paul, D. R.; Robeson, L. M. Polymer Nanotechnology: Nanocomposites. *Polymer* **2008**, *49*, 3187−3204.

(14) Kumar, S. K.; Benicewicz, B. C.; Vaia, R. A.; Winey, K. I. 50th Anniversary Perspective: Are Polymer Nanocomposites Practical for Applications? *Macromolecules* **2017**, *50*, 714−731.

(15) Jog, J.Crystallization in Polymer Nanocomposites. In *Optimization of Polymer Nanocomposite Properties*; John Wiley & Sons, Ltd., 2010; pp 279−300 DOI: 10.1002/9783527629275.ch13.

(16) Trujillo, M.; Arnal, M. L.; Müller, A. J.; Laredo, E.; Bredeau, S.; Bonduel, D.; Dubois, P. Thermal and Morphological Characterization of Nanocomposites Prepared by In-Situ Polymerization of High-Density Polyethylene on Carbon Nanotubes. *Macromolecules* **2007**, *40*, 6268−6276.

(17) Müller, A. J.; Arnal, M. L.; Trujillo, M.; Lorenzo, A. T. Super-Nucleation in Nanocomposites and Confinement Effects on the Crystallizable Components within Block Copolymers, Miktoarm Star Copolymers and Nanocomposites. *Eur. Polym. J.* **2011**, *47*, 614−629.

(18) Sinha Ray, S.; Okamoto, M. Polymer/Layered Silicate Nanocomposites: A Review from Preparation to Processing. *Prog. Polym. Sci.* **2003**, *28*, 1539−1641.

(19) Wu, R.; Wang, S.; Leng, Y.; Li, Q. Preparation, Structure, and Properties of Poly(Ethyleneoxide)/Lignin Composites Used for UV Absorption. *J. Appl. Polym. Sci.* **2020**, *137*, 48593.

(20) Jędrzejczak, P.; Puszka, A.; Kubiak, A.; Podkościelna, B.; Klapiszewski, Ł. New Lignin-Based Hybrid Materials as Functional Additives for Polymer Biocomposites: From Design to Application. *Int. J. Biol. Macromol.* **2021**, *190*, 624−635.

(21) Yu, P.; He, H.; Jia, Y.; Tian, S.; Chen, J.; Jia, D.; Luo, Y. A Comprehensive Study on Lignin as a Green Alternative of Silica in Natural Rubber Composites. *Polym. Test.* **2016**, *54*, 176−185.

(22) Collins, M. N.; Nechifor, M.; Tanasă, F.; Zănoagă, M.; McLoughlin, A.; Stróżyk, M. A.; Culebras, M.; Teacă, C. A.Valorization of Lignin in Polymer and Composite Systems for Advanced Engineering Applications − A Review. In *International Journal of Biological Macromolecules*, Elsevier B.V., 2019; pp 828−849 DOI: 10.1016/j.ijbiomac.2019.03.069.

(23) Shah, T.; Gupta, C.; Ferebee, R. L.; Bockstaller, M. R.; Washburn, N. R. Extraordinary Toughening and Strengthening Effect in Polymer Nanocomposites Using Lignin-Based Fillers Synthesized by ATRP. *Polymer* **2015**, *72*, 406−412.

(24) Papageorgiou, G. Z.; Karandrea, E.; Giliopoulos, D.; Papageorgiou, D. G.; Ladavos, A.; Katerinopoulou, A.; Achilias, D. S.; Triantafyllidis, K. S.; Bikiaris, D. N. Effect of Clay Structure and Type of Organomodifier on the Thermal Properties of Poly (Ethylene Terephthalate) Based Nanocomposites. *Thermochim. Acta* **2014**, *576*, 84−96.

(25) Papadopoulos, L.; Klonos, P. A.; Terzopoulou, Z.; Psochia, E.; Sanusi, O. M.; Hocine, N. A.; Benelfellah, A.; et al. Comparative Study of Crystallization, Semicrystalline Morphology, and Molecular Mobility in Nanocomposites Based on Polylactide and Various Inclusions at Low Filler Loadings. *Polymer* **2021**, *217*, No. 123457.

(26) Kumar, S. K.; Jouault, N.; Benicewicz, B.; Neely, T. Nanocomposites with Polymer Grafted Nanoparticles. *Macromolecules* **2013**, *46*, 3199−3214.

(27) Kadla, J. F.; Kubo, S. Miscibility and Hydrogen Bonding in Blends of Poly(Ethylene Oxide) and Kraft Lignin. *Macromolecules* **2003**, *36*, 7803−7811.

(28) Kubo, S.; Kadla, J. F. Poly(Ethylene Oxide)/Organosolv Lignin Blends: Relationship between Thermal Properties, Chemical Structure, and Blend Behavior. *Macromolecules* **2004**, *37*, 6904−6911.

(29) Jayaramudu, T.; Ko, H. U.; Kim, H. C.; Kim, J. W.; Choi, E. S.; Kim, J. Adhesion Properties of Poly(Ethylene Oxide)-Lignin Blend for Nanocellulose Composites. *Composites, Part B* **2019**, *156*, 43−50.

(30) Wen, X.; Su, Y.; Liu, G.; Li, S.; Müller, A. J.; Kumar, S. K.; Wang, D. Direct Relationship between Dispersion and Crystallization Behavior in Poly(Ethylene Oxide)/Poly(Ethylene Glycol)-g-Silica Nanocomposites. *Macromolecules* **2021**, *54*, 1870−1880.

(31) Pérez, R. A.; López, J. V.; Hoskins, J. N.; Zhang, B.; Grayson, S. M.; Casas, M. T.; Puiggalí, J.; Müller, A. J. Nucleation and Antinucleation Effects of Functionalized Carbon Nanotubes on

Cyclic and Linear Poly(ε-Caprolactones). *Macromolecules* **2014**, *47*, 3553−3566.
(32) Altorbaq, A. S.; Krauskopf, A. A.; Wen, X.; Pérez-Camargo, R. A.; Su, Y.; Wang, D.; Müller, A. J.; Kumar, S. K. Crystallization Kinetics and Nanoparticle Ordering in Semicrystalline Polymer Nanocomposites. *Prog. Polym. Sci.* **2022**, *128*, No. 101527.
(33) Xu, J. Z.; Zhang, Z. J.; Xu, H.; Chen, J. B.; Ran, R.; Li, Z. M. Highly Enhanced Crystallization Kinetics of Poly(l -Lactic Acid) by Poly(Ethylene Glycol) Grafted Graphene Oxide Simultaneously as Heterogeneous Nucleation Agent and Chain Mobility Promoter. *Macromolecules* **2015**, *48*, 4891−4900.
(34) Habel, C.; Maiz, J.; Olmedo-Martínez, J. L.; López, J. V.; Breu, J.; Müller, A. J. Competition between Nucleation and Confinement in the Crystallization of Poly(Ethylene Glycol)/ Large Aspect Ratio Hectorite Nanocomposites. *Polymer* **2020**, *202*, No. 122734.
(35) Jimenez, A. M.; Altorbaq, A. S.; Müller, A. J.; Kumar, S. K. Polymer Crystallization Under Confinement by Well-Dispersed Nanoparticles. *Macromolecules* **2020**, *53*, 10256−10266.
(36) Altorbaq, A. S.; Jimenez, A. M.; Pribyl, J.; Benicewicz, B.; Mü, A. J.; Kumar, S. K. Polymer Spherulitic Growth Kinetics Mediated by Nanoparticle Assemblies. *Macromolecules* **2021**, *54*, 1063−1072.
(37) Taverna, M. E.; Busatto, C. A.; Lescano, M. R.; Nicolau, V. V.; Zalazar, C. S.; Meira, G. R.; Estenoz, D. A. Microparticles Based on Ionic and Organosolv Lignins for the Controlled Release of Atrazine. *J. Hazard. Mater.* **2018**, *359*, 139−147.
(38) Pérez-Camargo, R. A.; Liu, G. M.; Wang, D. J.; Müller, A. J. Experimental and Data Fitting Guidelines for the Determination of Polymer Crystallization Kinetics. *Chinese J. Polym. Sci.* **2022**, *40*, 658−691.
(39) Fillon, B.; Lotz, B.; Thierry, A.; Wittmann, J. C. Self-nucleation and Enhanced Nucleation of Polymers. Definition of a Convenient Calorimetric "Efficiency Scale" and Evaluation of Nucleating Additives in Isotactic Polypropylene (α Phase). *J. Polym. Sci., Part B: Polym. Phys.* **1993**, *31*, 1395−1405.
(40) Fillon, B.; Wittmann, J. C.; Lotz, B.; Thierry, A. Self-Nucleation and Recrystallization of Isotactic Polypropylene (α Phase) Investigated by Differential Scanning Calorimetry. *J. Polym. Sci., Part B: Polym. Phys.* **1993**, *31*, 1383−1393.
(41) Fillon, B.; Thierry, A.; Lotz, B.; Wittmann, J. C. Efficiency Scale for Polymer Nucleating Agents. *J. Therm. Anal.* **1994**, *42*, 721−731.
(42) Schneider, C. A.; Rasband, W. S.; Eliceiri, K. W. NIH Image to ImageJ: 25 Years of Image Analysis. *Nat. Methods* **2012**, *9*, 671−675.
(43) Pang, Y.; Wang, S.; Qiu, X.; Luo, Y.; Lou, H.; Huang, J. Preparation of Lignin/Sodium Dodecyl Sulfate Composite Nanoparticles and Their Application in Pickering Emulsion Template-Based Microencapsulation. *J. Agric. Food Chem.* **2017**, *65*, 11011−11019.
(44) Fernández-d'Arlas, B.; Baumann, R. P.; Pöselt, E.; Müller, A. J. Influence of Composition on the Isothermal Crystallisation of Segmented Thermoplastic Polyurethanes. *CrystEngComm* **2017**, *19*, 4720−4733.
(45) Martínez-Vázquez, D. G.; Medellín-Rodríguez, F. J.; Phillips, P. J.; Sanchez-Valdes, S. Heterogeneous Nucleation of Nylon 6 and PET with Selected Inorganic Compounds. *J. Appl. Polym. Sci.* **2003**, *88*, 360−368.
(46) Price, F. P.Nucleation in Polymer Crystallization. In *Nucleation*; Zettlemoyer, A. C., Ed.; Marcel Dekker, 1969; pp 405−488.
(47) Beaumont, R. H.; Clegg, B.; Gee, G.; Herbert, J. B. M.; Marks, D. J.; Roberts, R. C.; Sims, D. Heat Capacities of Propylene Oxide and of Some Polymers of Ethylene and Propylene Oxides. *Polymer* **1966**, *7*, 401−417.
(48) Jimenez, A. M.; Krauskopf, A. A.; Pérez-Camargo, R. A.; Zhao, D.; Pribyl, J.; Jestin, J.; Benicewicz, B. C.; Müller, A. J.; Kumar, S. K. Effects of Hairy Nanoparticles on Polymer Crystallization Kinetics. *Macromolecules* **2019**, *52*, 9186−9198.
(49) Pérez-Camargo, R. A.; Saenz, G.; Laurichesse, S.; Casas, M. T.; Puiggalí, J.; Avérous, L.; Müller, A. J. Nucleation, Crystallization, and Thermal Fractionation of Poly (ε-Caprolactone)-Grafted-Lignin: Effects of Grafted Chains Length and Lignin Content. *J. Polym. Sci., Part B: Polym. Phys.* **2015**, *53*, 1736−1750.
(50) Lauritzen, J. I.; Hoffman, J. D. Formation of Polymer Crystals with Folded Chains from Dilute Solution. *J. Chem. Phys.* **1959**, *31*, 1680−1681.
(51) Hoffman, J. D.; Lauritzen, J. I. Crystallization of Bulk Polymers with Chain Folding: Theory of Growth of Lamellar Spherulites. *J. Res. Natl. Bur. Stand. Sect., A* **1961**, *65A*, 297.
(52) Bornani, K.; Rahman, M. A.; Benicewicz, B.; Kumar, S.; Schadler, L. Using Nanofiller Assemblies to Control the Crystallization Kinetics of High-Density Polyethylene. *Macromolecules* **2021**, *54*, 5673−5682.
(53) VOGEL, H. Das Temperaturabhangigkeitsgesetz Der Viskositat von Flussigkeiten. *Phys. Z.* **1921**, *22*, 645−646.
(54) Fulcher, G. S. Analysis of Recent Measurements of the Viscosity of Glasses. *J. Am. Ceram. Soc.* **1992**, *75*, 1043−1055.
(55) Tammann, G.; Hesse, W. Die Abhängigkeit Der Viscosistat von Der Temperatur Bei Unterkühlten Flüssigkeiten'. *Z. Anorg. Allg. Chem.* **1926**, *156*, 245−257.
(56) Armistead, J. P.; Hoffman, J. D. Direct Evidence of Regimes I, II, and III in Linear Polyethylene Fractions As Revealed by Spherulite Growth Rates. *Macromolecules* **2002**, *35*, 3895−3913.
(57) Hoffman, J. D.; Miller, R. L. Kinetic of Crystallization from the Melt and Chain Folding in Polyethylene Fractions Revisited: Theory and Experiment. *Polymer* **1997**, *38*, 3151−3212.
(58) Nitta, K. hei.; Asuka, K.; Liu, B.; Terano, M. The Effect of the Addition of Silica Particles on Linear Spherulite Growth Rate of Isotactic Polypropylene and Its Explanation by Lamellar Cluster Model. *Polymer* **2006**, *47*, 6457−6463.
(59) Trujillo, M.; Arnal, M. L.; Müller, A. J.; Mujica, M. A.; Urbina De Navarro, C.; Ruelle, B.; Dubois, P. Supernucleation and Crystallization Regime Change Provoked by MWNT Addition to Poly(ε-Caprolactone). *Polymer* **2012**, *53*, 832−841.
(60) Gumede, T. P.; Luyt, A. S.; Pérez-Camargo, R. A.; Tercjak, A.; Müller, A. J. Morphology, Nucleation, and Isothermal Crystallization Kinetics of Poly(Butylene Succinate) Mixed with a Polycarbonate/ MWCNT Masterbatch. *Polymers* **2018**, *10*, No. 424.
(61) Li, Y.-D.; Li, H.; Du, A.-K.; Wang, M.; Zeng, J.-B. Morphology and Isothermal Crystallization of Graphene Oxide Reinforced Biodegradable Poly (Butylene Succinate). *Polym. Test.* **2017**, *59*, 1−9.
(62) Vega, J. F.; Fernández-Alcázar, J.; López, J. V.; Michell, R. M.; Pérez-Camargo, R. A.; Ruelle, B.; Martínez-Salazar, J.; Arnal, M. L.; Dubois, P.; Müller, A. J. Competition between Supernucleation and Plasticization in the Crystallization and Rheological Behavior of PCL/ CNT-Based Nanocomposites and Nanohybrids. *J. Polym. Sci., Part B: Polym. Phys.* **2017**, *55*, 1310−1325.
(63) Lorenzo, A. T.; Müller, A. J. Estimation of the Nucleation and Crystal Growth Contributions to the Overall Crystallization Energy Barrier. *J. Polym. Sci., Part B: Polym. Phys.* **2008**, *46*, 1478−1487.
(64) Avrami, M. Granulation, Phase Change, and Microstructure Kinetics of Phase Change. III. *J. Chem. Phys.* **1941**, *9*, 177−184.
(65) Balsamo, V.; Urdaneta, N.; Pérez, L.; Carrizales, P.; Abetz, V.; Müller, A. J. Effect of the Polyethylene Confinement and Topology on Its Crystallisation within Semicrystalline ABC Triblock Copolymers. *Eur. Polym. J.* **2004**, *40*, 1033−1049.
(66) Michell, R. M.; Müller, A. J. Confined Crystallization of Polymeric Materials. *Prog. Polym. Sci.* **2016**, *54*−*55*, 183−213.
(67) Zhao, W.; Su, Y.; Wen, X.; Wang, D. Manipulating Crystallization Behavior of Poly(Ethylene Oxide) by Functionalized Nanoparticle Inclusion. *Polymer* **2019**, *165*, 28−38.

https://doi.org/10.1021/acs.macromol.2c00925
Macromolecules 2022, 55, 7663−7673